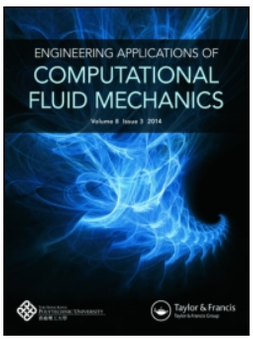

Engineering Applications of Computational Fluid Mechanics

ISSN: 1994-2060 (Print) 1997-003X (Online) Journal homepage: https://www.tandfonline.com/loi/tcfm20

Experimental and numerical study of turbulent flow around a Fanwings profile

Slimane Benferhat, Tayeb Yahiaoui, Bachir Imine, Omar Ladjedel & Ondřej Šikula

To cite this article: Slimane Benferhat, Tayeb Yahiaoui, Bachir Imine, Omar Ladjedel & Ondřej Šikula (2019) Experimental and numerical study of turbulent flow around a Fanwings profile, Engineering Applications of Computational Fluid Mechanics, 13:1, 698-712, DOI: 10.1080/19942060.2019.1639076

To link to this article: https://doi.org/10.1080/19942060.2019.1639076

Published online: 20 Jul 2019.

ENGINEERING APPLICATIONS OF COMPUTATIONAL FLUID MECHANICS
2019, VOL. 13, NO. 1, 698–712
https://doi.org/10.1080/19942060.2019.1639076

Taylor & Francis
Taylor & Francis Group

Experimental and numerical study of turbulent flow around a Fanwings profile

Slimane Benferhat[a], Tayeb Yahiaoui[a], Bachir Imine[a], Omar Ladjedel[b] and Ondřej Šikula[b]

[a]Laboratory Aeronautics and Propulsive Systems, Département de Génie Mécanique, Faculté de Génie Mécanique, University of Science and Technology of Oran Mohamed Boudiaf, Oran, Algeria; [b]Faculty of Civil Engineering, Brno University of Technology, Brno, Czechia

ABSTRACT

The main objective of this paper is an experimental and numerical study of airflow on a propulsive wing also called ventilated wing or FANWING, which is a drone operating at low speed. To optimize the aerodynamic shape of the Fanwing, two different configurations of NACA4415 rectangular wing profile were realized. The first one is a wing where the Cross-Flow Fan is fitted directly to the leading edge with a classic niche. For the second one, we truncated the extension of the niche to create a profile without nose. Two flow velocities with constant fan rotation were used and observed in the range of $-16° < \alpha < +30°$. A lift coefficient generated by the profiles increases and the drag coefficient decreases, while the distribution of the pressure coefficient on the upper surface increases abruptly because of the flow recirculation. The experiment was performed in a subsonic wind tunnel TE44 and numerical simulations in software Fluent 6.3.2.6. Both approaches are in good agreement. The visualization showed that the recirculation phenomenon occurs right after the discharge of the cross-flow fan. It reveals that the jet coming out of the fan causes a strong wake behind the profile and suppresses the boundary layer separation.

ARTICLE HISTORY
Received 21 March 2019
Accepted 29 June 2019

KEYWORDS
Fanwing; aerodynamics; recirculation; eccentric vortex

1. Introduction

The physical study of the flow around the profiles is of great interest in understanding its behavior in order to predict the phenomenon of dynamic stall and stability. These flows are complex and irregular generating swirling flows that can be detrimental in internal flows causing vibrations and system damage. They also can be beneficial in external flows such as cooling or in aeronautics, producing lift in rotary wing aircrafts. The rotational flows are always captivating whether they are from a convective flow, generating a hurricane or formed by using a turbomachine or a rotor. One of these devices is the cross-flow fan, where the air is sucked by the cross-flow fan and then stirred with the blades. The whirling air gives birth to a vortex inside the fan before being ejected radially. This vortex is eccentric. Its position and dynamics quantitatively affect the overall characteristics of the device (Element 2, Figure 1). The majority of the work carried out on Cross-Flow Fans is generally experimental, aimed at improving the aerodynamic performance. By modifying the geometric characteristics randomly, guided either by the stability of the system or by its size. Several research projects are the subject of intensive studies on its application in aeronautics. A detailed understanding of this flow field is essential.

For several years, the improved performance of rotorcrafts and rotary wing aircrafts capable of vertical takeoff and landing (VTOL) or a short takeoff and landing (STOL), has led research to innovation and the Fanwing is one. He requires a short runway. The novelty of this type of propulsion is to move an aircraft using a cylindrical fan. Fanwing is a rare concept, working at low Reynolds numbers, developed and patented by Peebles (2001); it was inspired by the paddle steamers that sailed the Mississippi River. This type of aircraft with motorized lift uses a turbine engine mounted on the entire wingspan of a wing similar to a rigid wing. This is a different mode of operation from the conventional aircraft. This type of turbomachine is called cross-flow fan. It was patented by Mortier (1893). The rotation of the fan is used to accelerate the air flow on the profile.

This action results in lift and propulsion while delaying the boundary layer separation, stemming from the acceleration of the incoming air and entering from the leading edge directed towards the trailing edge.

The evolution of computer tools and digital methods has revolutionized the CFD. It has had an impact on fluid mechanics and aerodynamics flows. The development of this tool has enabled computational fluid dynamics to cover all domains related to fluid flows

CONTACT Ondřej Šikula sikula.o@vutbr.cz

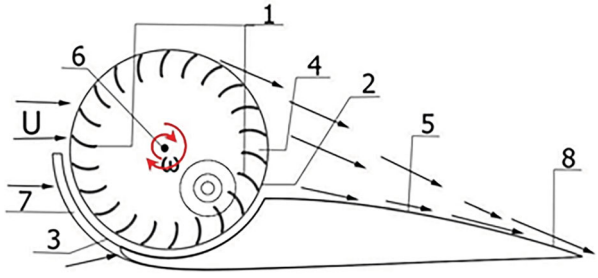

Figure 1. Flow around Fanwing with à modified Naca 4415 profile.

(internal and external). From architecture for building construction (Mou, He, Zhao, & Chau, 2017) to hydrogen production (Akbarian et al., 2018) to internal engine flows (Ardabili et al., 2018) to Nano-fluid (Ramezanizadeh, Nazari, Ahmadi, & Chau, 2018), (Ghalandari, Koohshahi, Mohamadian, Shamshirband, & Chau, 2019). This revolution has led to the emergence of digital aerodynamics, which plays a role in the design and optimization of aircraft.

1.1. Principle of operation of the Fanwing

The rotation of the blades (1), of the rotor (2) placed in the cavity (3) accelerates the air sucked in. It passes twice between the blades (4) (which transmits to the air its energy) where about 2/3 of the rotor diameter exceeds the upper surface of the profile and then directs the flow towards the rear of the upper surface (5). Which produce lift and propulsion simultaneously. They depend on the speed of rotation ω of the axis (6) while delaying the boundary layer separation resulting from the acceleration of the air. Depending on the shape of the leading edge (7) the air flow will be regulated and the lift and propulsion forces will be controlled. The trailing edge (8) forces the flow to be parallel to its plane (Coanda Effect) (Figure 1). This results in unusual aerodynamic parameters and specific qualities with a broad operating prospect.

In collaboration with Peebles, Forshaw (1999) conducted the first basic Fanwing investigation at the Imperial College of London, where the experimental study was performed in the college's wind tunnel. He showed that the lift increases by 50% compared to a conventional aircraft and does not stall even at high angles of attack. Kogler (2000) continued the experiment on the same prototype. He noticed that the Fanwing works well at low altitude, contrary to the observations of Forshaw.

Kogler found that the wing was stalling for angles of attack above 20 degrees and suggested that in order to avoid the stall, it is necessary to have additional engine power. Modifying Peebles profile, Duddempudi, Yao, Edmondson, Yao, and Curley (2007) performs a new numerical simulation while reducing the thickness by 16 mm. She concludes that the results are comparable to those obtained by Kogler and predicts that the lift force is close with an error of about 6.55%, and the drag force is comparable to 12.59%. Both of these errors are generally acceptable. With the modified geometry, the refinement of the fineness increases by about 29.42%. She states that the stall occurs at higher angles of incidence and the position of the eccentric vortex inside the fan is the key element.

Several studies on cross-flow fans were done. Toffolo (2005) observes an eccentric vortex formation inside the cross-flow fan, similar to that found in studies established on the same devices. The position of the eccentric vortex on the inside is the most important phenomenon to define these aerodynamic parameters. Tanaka and Murata (1994) noticed that the flow inside the fan is very complicated and difficult to predict the behavior. The numerical study makes it possible to evaluate these aerodynamic performances, as well as the flow details in particular in the center with more accuracy. However, Mazur (1984) concludes that the geometry of the cavity of the fan is more important than the parameters of the fan (Moon, Cho, & Nam, 2003). describe the Fanwing as a flying lawn mower. The similarity is the use of a tangential fan mounted along the leading edge of the wing. They state that in addition to the increase of the coefficient of lift CL, the fan generates a thrust force that accelerates the flow of air towards the trailing edge. This phenomenon delays the boundary layer separation and the stall occurs at an incidence greater than 30°.

Kentfield (2005) believes that, to obtain stability at high altitudes it would be necessary to add to the Fanwing drifts (equip the Fanwing with winglets on the wing and the tail of the aircraft) in order to avoid great moments of roll and the boundary layer separation which causes wingtip vortices. This addition allowed the Fanwing to hover and expand flight speeds and reduced its sound. To have the ability to fly slowly and safely in urban areas, it would only need a short runway for takeoff or landing. Its low sonority at low altitude allows effective monitoring at the times of peace, war or emergency situations (Douglas & Geoff, 2009).

When Ahad and Graham (2007) conducted flight tests of the Fanwing model, working on the model of Forshaw (1999) they determined that even if the aircraft did not fly under the conditions of a real plane, the tests are conclusive. The takeoff and landing distances are shorter, compared to conventional aircraft. By adding drifts on the wings to reduce the pitching moment they almost doubled their cruising speed and the model has more of

a stable behavior. They also estimate a critical threshold of use between $-20° < \alpha < +20°$.

Saracoglu and Paniagua (2015) concluded that the static pressure inside the cavity is relatively low, compared to the upper surface caused by the presence of the eccentric vortex inside the fan. When increasing the rotational speed increases the lift and thrust proportionally to the mass flow of air forced through the fan on the wing surface.

According to Askari and Shojaeefard (2015), the improvement of the coefficient of pitch moment shows that the aircraft is more stable at higher rotational speeds.

In his investigation, Seyfang (2011) states that the development of Fanwing has considerably increased the cruising speed. This investigation focused on the comparison of four different rotorcrafts. It showed that the Fanwing requires a very short take-off runway and offers an interesting performance, similar to that of helicopters and inclined rotor aircrafts.

Kummer and Dang (2006) carried out another design by wake ingestion. Leroy and Smith (1993) demonstrated that, if a fan is placed behind a moving body, it absorbs the wake by re-energizing its flow. As a result, Kummer and Dang (2006) developed it, by working on a Gottingen 570 profile, they eliminated the fan support structure by enclosing the fan and installing it at the trailing edge. The fan recovers the energy of the flow by sucking its wake, allowing it to reduce the power of propulsion by saving the energy of the engine.

In 2010, Kummer, the Syracuse project and NASA, built a prototype of the Fanwing. Using CFD to solve Navier-Stokes 3D equations, a new polyhedral honeycomb mesh was invented to optimize fan housing and computation time.

2. Description of the solution

2.1. Experimental apparatus

The experimental tests were carried out in the TE 44 closed circuit horizontal atmospheric wind tunnel at USTO Oran (Figure 2(a)). The test section of the wind tunnel is square 0.46 m × 0.46, and 1.2 m long. It is of a classic design where the speed can reach 60 m/s. The intensity of the turbulence is less than 1% (Technical document).

Designed to measure the aerodynamic forces exerted on the profile, the wind tunnel is equipped with a TE 81 balance, connected by cables to strain gauges for the measurement of the lift, drag and pitch moment (Figure 2(d)). These will be read using the DATA SLIM software on the visualization interface shown in Figure 2(e) (the application software displays the pressure tapping points and the forces detected by the TE81 scale). For the pressure measurement, the machine is equipped with a TE44 DPS type sensor, which allows the recording of 20 static pressure taps of the flow. The experimental models in the test sections are shown in Figure 2(b,c).

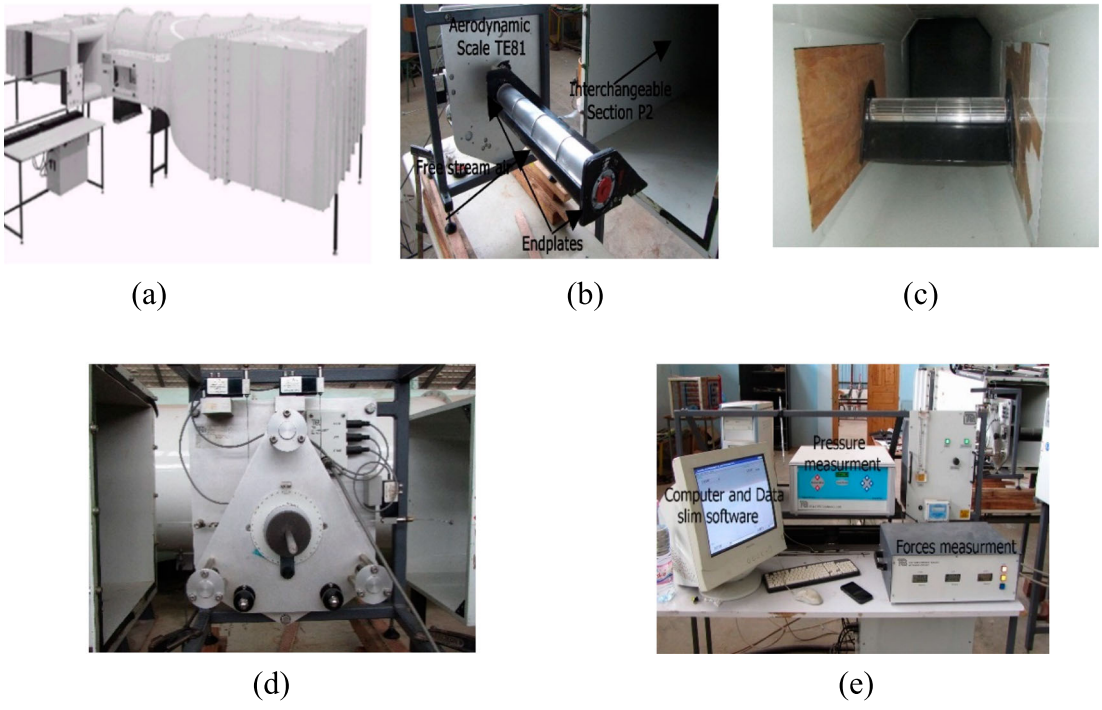

Figure 2. Experimental tests of Fanwing in USTO Oran. (a) Subsonic Wind tunnel TE44. (b) Free test section. (c) Closed test section. (d) Wind tunnel balance TE 81 and free test section. (e) Forces & pressure measurement.

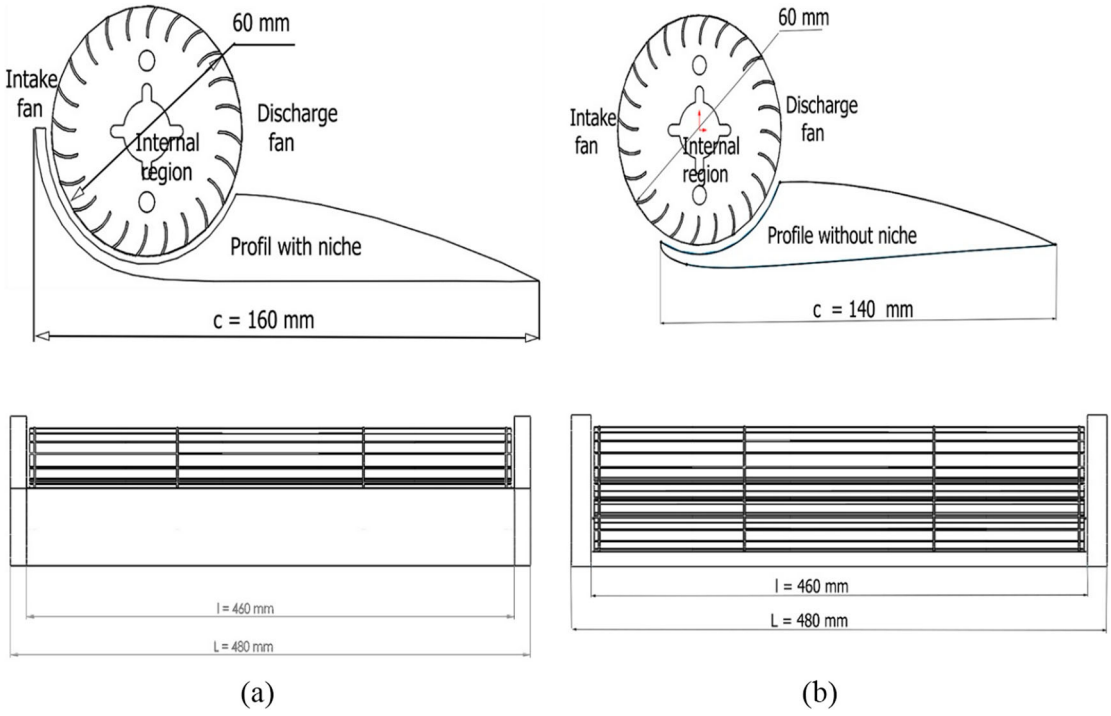

Figure 3. Fanwing study with à modified NACA 4415 profile. (a) Fanwing with niche. (b) Fanwing without niche.

2.2. Realization and description of the Fanwing models

The profile selection for low and high Reynolds numbers and for low and high altitudes led us to choose an asymmetric profile, (the NACA 4415). The latter is used for wide-body aircraft. Abbott and Von Doehoff (1959) performed a study on the aerodynamic performance of Naca 4415. He stated that the stall angle is more than 16° and that the drag is positive.

For our Fanwing study, the NACA 4415 profile is modified. The details shown in Figure 3(a,b) are drawn on SolidWorks, and the wings are constructed with Balsa aeromodelism wood.

The aluminum fan consists of 22 curved blades. The chord and the thickness of the blades are 10 and 0.4 mm respectively. The outer diameter of the fan is 60 mm (Figure 4, Element 6). For our design, conventional profiles such as the Naca 4415 limits the size of the fan for the support of the fastening system and for high-speed applications because of the compressibility effects. The cross-flow fan is likely to create a pressure difference allowing the flow of air between upstream and downstream. The cross flow-fan supplies to the air a large part of the mechanical energy that it receives through the electric motor shaft.

Figure 4 shows the different components of the test bench. To make the experimental tests more reliable and realistic. We used a PROTRONIK material intended

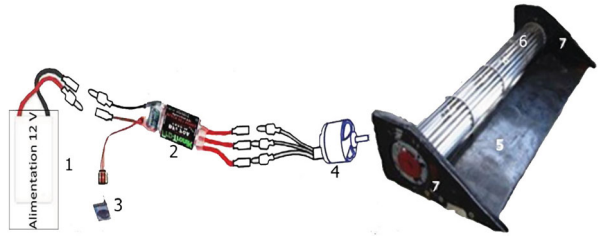

Figure 4. Components of the test bench.

for aeromodelism. The system consists of a three-phase 4000 rpm electric motor (4), directly coupled to a fan (6) of 440 mm in span and 60 mm in diameter. A six-position controller (3) and a 70-amp speed controller (2) are used to adjust the rotational speed and the desired power with an electrical circuit using a 12-volt power supply (1). The system is fixed on two supports (7) acting as fixing and endplate so that the flow is two-dimensional (2D). These experiments were carried out on two models of wings of infinite span $L = 460$ mm and two chords ($c = 160$ mm and $c = 140$ mm) for the profile with niche and profile without niche respectively.

The aerodynamic parameters were measured at a rotational speed of $n = 3000$ rpm and two Reynolds numbers $Re = 76{,}765$ and 57,574; hence the two-speed rates that define the ratio of the fan rotational speed and the airflow speed ($\Lambda = 1.55$ and $\Lambda = 1.18$). According to Kogler (2000), this is the key parameter of the Fanwing

similitude ratio Λ, i.e. two free stream velocity 7.98 and 6.07 m/s were used for the experimental study. This work is done at a range of incidence of $-16° < \propto < +30°$. The airflow on the profiles are the turbulent and the viscosity this is assumed unchanged throughout the study.

$$Re = \frac{U_\infty \cdot c}{\nu} \quad (1)$$

$$TSR = \Lambda = \frac{\omega r}{U_\infty} \quad (2)$$

2.3. Results and discussions of the experiments

2.3.1. Impacts of the fan rotational speed

Given the low efficiency at high speeds, the choice of tangential fan is one of the major concerns. Published work on fan performance is generally 40% for simple geometries and 60% for more complex ones (Mazur, 1984).

However, in Harloff's (1979) research, an efficacy of 70–80% was studied. The equipment available in the laboratory did not allow us to vary the rotation. However, in our investigation, Kogler (2000) and Askari and Shojaeefard (2015) claim that the coefficient of lift increases and the drag decreases rapidly. They are strongly influenced by the variation of the fan rotational speed. Saracoglu and Paniagua (2015) used a wide range of Tip Speed Ratio (Λ) and observed the effect of angular velocity. A significant increase in the lift and thrust coefficient was noted as a function of the increase in rotational speed. The lift coefficient reaches values up to 83 for very high rotational speeds, corresponding to peak speed ratios of approximately $\Lambda = 30$.

Several studies on aerodynamic performance using a Navier-Stokes solver have been conducted. In the research of Chen and Lian (2015), a numerical investigation of vortex dynamics in an H-rotor vertical axis wind turbine is done, they note that the dimensionless number tip speed ratio (Λ) defined the range of wind turbines and it can be seen that as the tip speed ratio (Λ) decreases more portion of the rotation cycle exceeds the static stall angle.

2.3.2. Influence of the Reynolds number

To define the aerodynamic parameters of a wing, we drew the curves of the lift and drag coefficients of the wing. Then, we observed the pressure coefficient on the profile.

(a) Lift coefficient

The values of ΔC_L, are injected on the C_L graphs to estimate the relative error. Note that these errors are small for positive impacts and increases for large values of negative angles.

In Figure 5, curves (a) and (b) represent the lift coefficient for the two Reynolds numbers. We note that it decreases as the Reynolds number increases. However, it is important to note that despite the fact that the lift coefficient is decreasing, the lift force increases when the Reynolds number is increased. This decrease of the lift

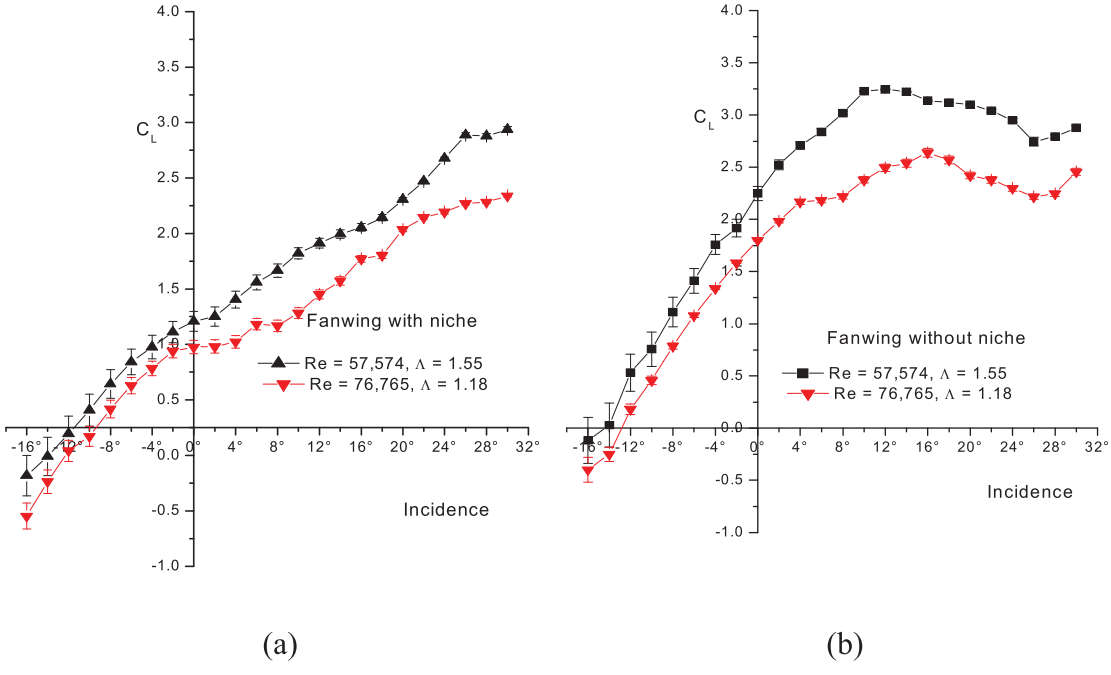

Figure 5. Variation of the lift coefficients of the two Fanwing profiles with the bars of the relative error.

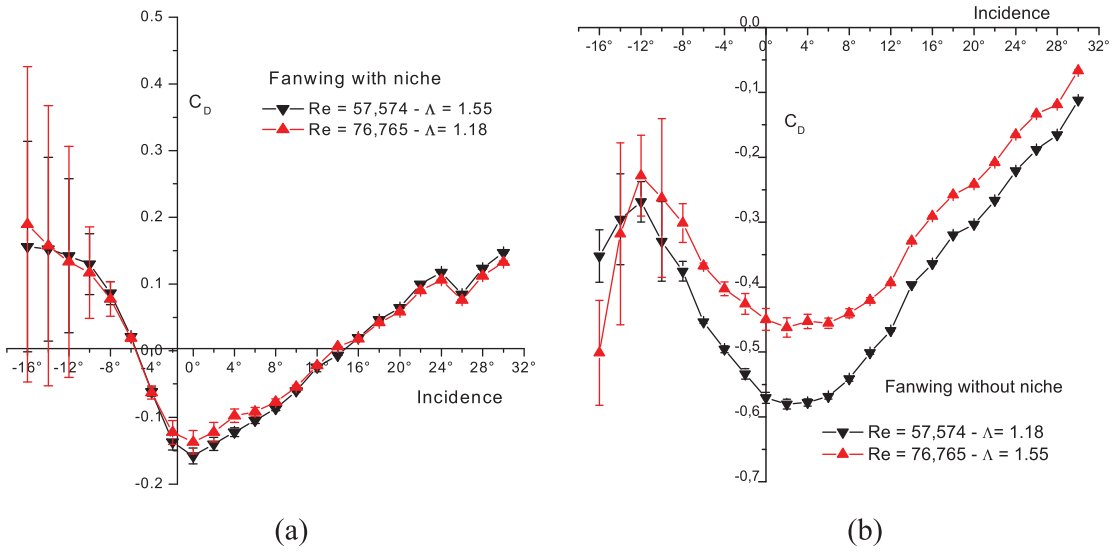

Figure 6. Variation of the drag coefficients of the two Fanwing profiles with the bars of the relative error.

coefficient results from the definition of lift, which is proportional to the square of flow velocity. At an incidence of 0°, the profile develops a high coefficient of lift; this is the characteristic of Fanwings. The C_L increases linearly with the angle of attack $C_L = C_L(\alpha)$, for the Fanwing without a niche. It reaches a maximum between the incidence of 8° and 14°, then suddenly drops; the flow no longer follows the shape of the profile.

$$C_L = \frac{2L}{\rho \cdot S \cdot U^2} \tag{3}$$

(b) Drag coefficient

The error values of the drag coefficients ΔC_D, are introduced on the C_D graphs. They are relatively low, as predicted for lift. It remains low for both profiles. It increases for negative angles (from $\alpha > -8$).

The drag coefficient graphs (a) and (b) in Figure 6 show that the profile drag is completely negative for the fanwing without niche. For $\propto = 0°$ the value of $C_D = -0.57756$. It acts as a propulsive force and it is the rotation of the fan that reduces it to become negative.

While for fanwing with niche the C_D values are low. For $\propto = 0°$ the value of $C_D = -0.15773$. And can be used between $-4° \leq \propto \leq +14°$.

The drag goes through a minimum where the propulsive force is maximum, and then it varies until it becomes maximum where the propulsive force becomes minimal. For high incidences, the motor weakens and requires an increase in power to produce the necessary propulsive force. By taking more incidence (positive angle) the fan of the profile without niche drops speed. It encounters air resistance and the speed of rotation of the cross-flow fan decreases. To keep it constant at 3000 rpm increases the electrical energy of the motor.

$$C_D = \frac{2D}{\rho \cdot S \cdot U^2} \tag{4}$$

The curves of the lift coefficient in Figure 7(a) represent the profile without niche, which is more advantageous than that with niche. They show that, even with negative incidence, the Fanwing is stable and produces a lift at −10°. Then the lift coefficient increases almost linearly with the angle of attack and reaches a maximum of +20° where it drops. The flow no longer follows the shape of the profile; it is the phenomenon of stalling.

For high Reynolds numbers, the lift coefficient can be smaller whereas the lift force is higher, and for low Reynolds numbers and longer monitoring and interesting, and for higher speeds the consumption of energy will be more significant.

It follows from the curves of the drag coefficient of Figure 7(b) that the drag force generated by the profile increases with the Reynolds number and decreases with the rotation of the fan, until it becomes propulsion. This brings us to the goal we are seeking a low Reynolds surveillance aircraft. They show that the profile with niche has more resistance to air than that without a niche, therefore produces more drag than propulsion. This is attributed to the geometry of the fan cavity as claims Mazur (1984), it is the most important parameter. The drag coefficient decreases with the Reynolds number, while the drag force itself increases in the same way as the lift.

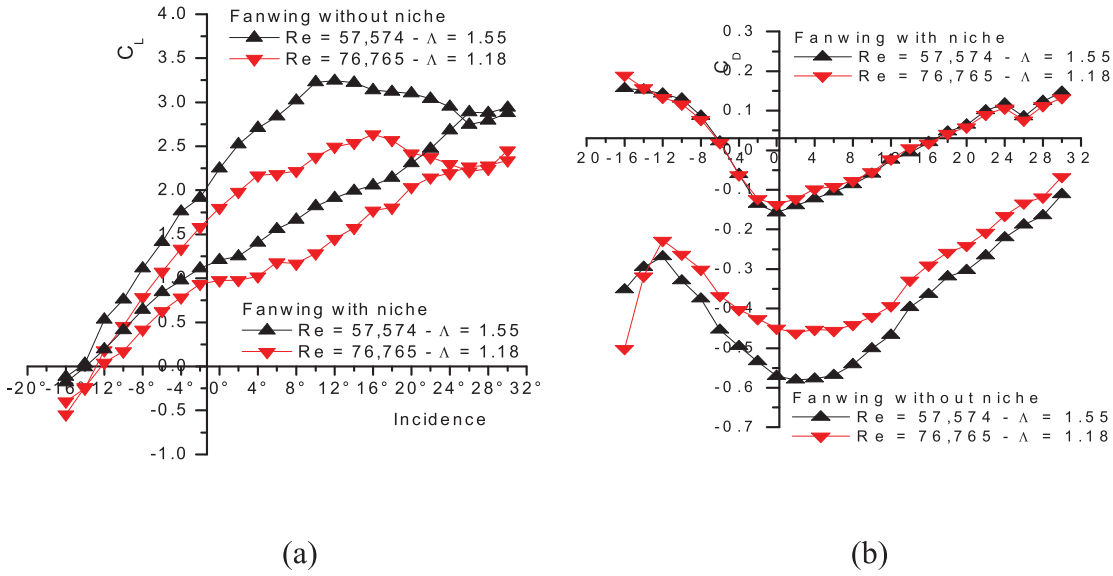

Figure 7. Comparison of the variation of lift and drag coefficients between the two Fanwing profiles.

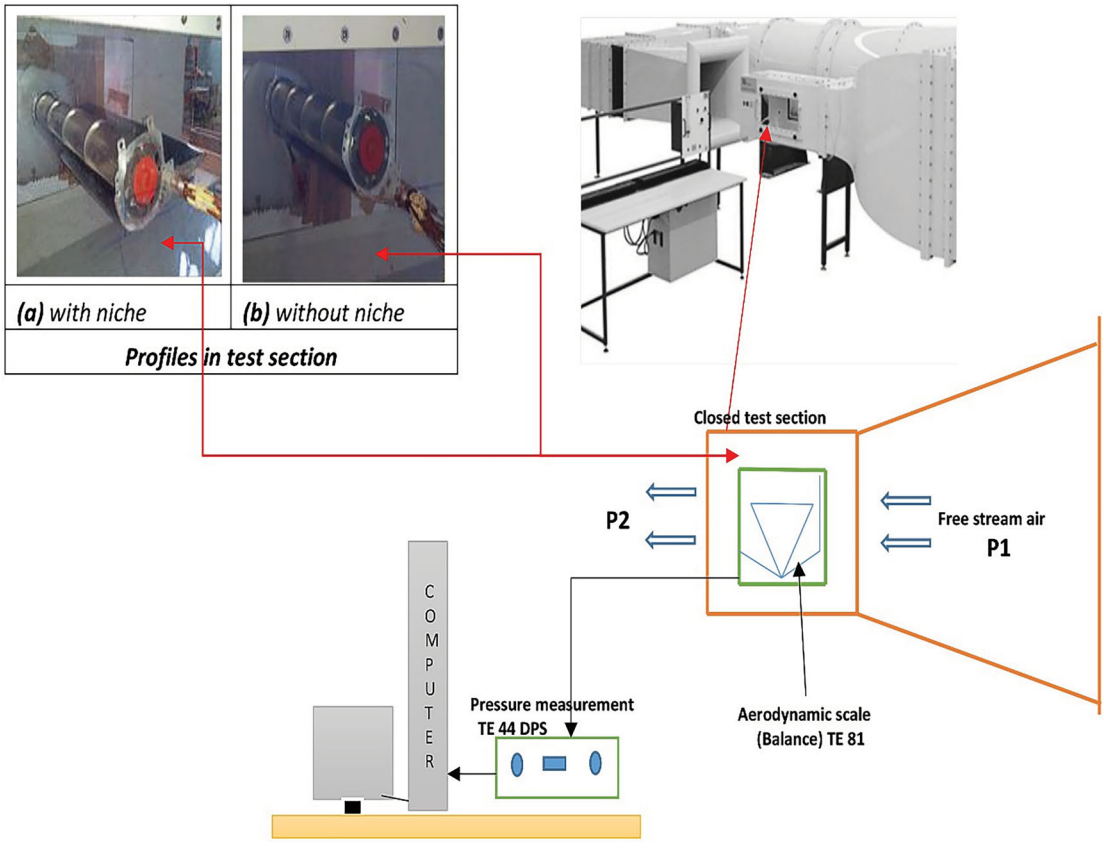

Figure 8. Positioning of the profiles in the closed test section for pressure coefficient measurement.

(c) Pressure coefficient

As shown in Figure 8, the location of the profiles in the closed test section for the measurement of the pressure coefficient. The shapes shown on the curves of Figures 9 and 10 illustrate the comparison of the distribution of the pressure coefficient at different incidences. Much of the lift occurs in the cavity by the effect of the rotation that is defined by the Magnus effect. We can see the evolution of the pressure gradient as well as the pressure jump observed on the upper surface of the Fanwing without niche, at the very beginning of the discharge of

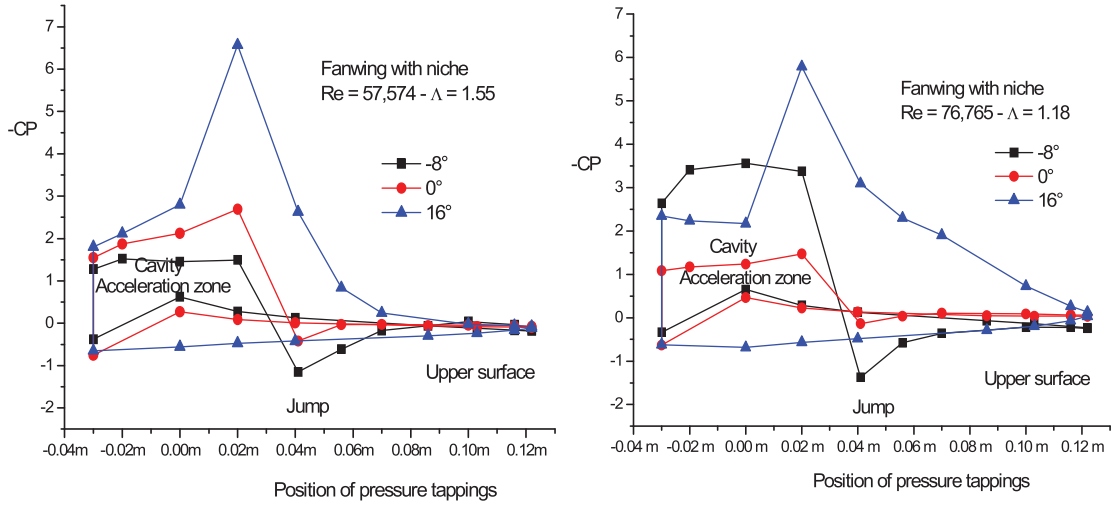

Figure 9. Distribution of the pressure coefficient of the Fanwing with niche.

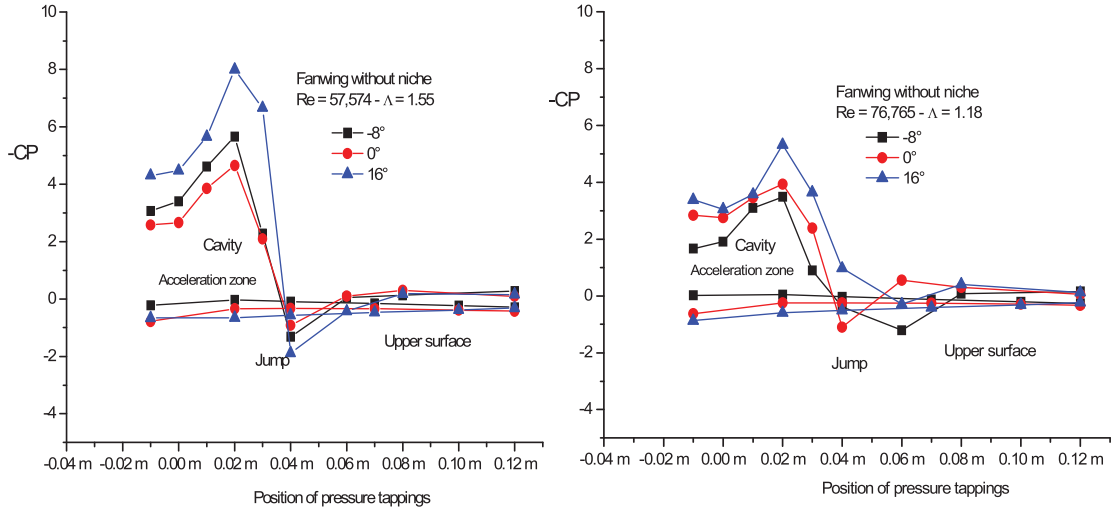

Figure 10. Distribution of the pressure coefficient of the Fanwing without niche.

the fan.

$$C_P = \frac{p - p_\infty}{(1/2)\rho U_\infty^2} \tag{5}$$

We deduce from this series of curves (Figure 11) that a stagnation point appears with a sudden jump in pressure on the upper surface of the profiles. Overall, even if they are similar in shape, the Fanwing with niche does not develop an important pressure gradient. Unlike the Fanwing without niche for which it is considerable along the entire profile and which is reflected on the lift. This jump is due to the geometry of the cavity and the sharp edge on the profile. To reduce this jump, Askari and Shojaeefard (2015) claims that the sharp edge is replaced by a smooth rounded edge.

If the depression gap becomes important, there will be a risk of developing a critical speed that will give rise to a deformation of the wing. It is proposed to install a perforated deflector with variable opening to control the airflow. We can see that the distribution of the pressure coefficient depends on the geometry of the housing and that the profile without niche has large negative pressure values and develops large lift coefficients.

2.4. Observation of the flow by visualization

The visualization was performed on the wing without niche at an incidence of zero (0°) and five (5°) degrees and at a $\Lambda = 1.55$ and $Re = 57{,}574$, which aims to observe the flow and locate the eccentric vortex inside the Cross Flow Fan, as well as the wake at the exit of the fan (Figure 12(a)).

During the flow, a jet of smoke is initiated towards the fan. It passes first through the intake fan of the cross-flow fan (Figure 3) and then into the inner region of the fan, where the eccentric vortex is formed by the action of the blades on the fluid supplied by the motor

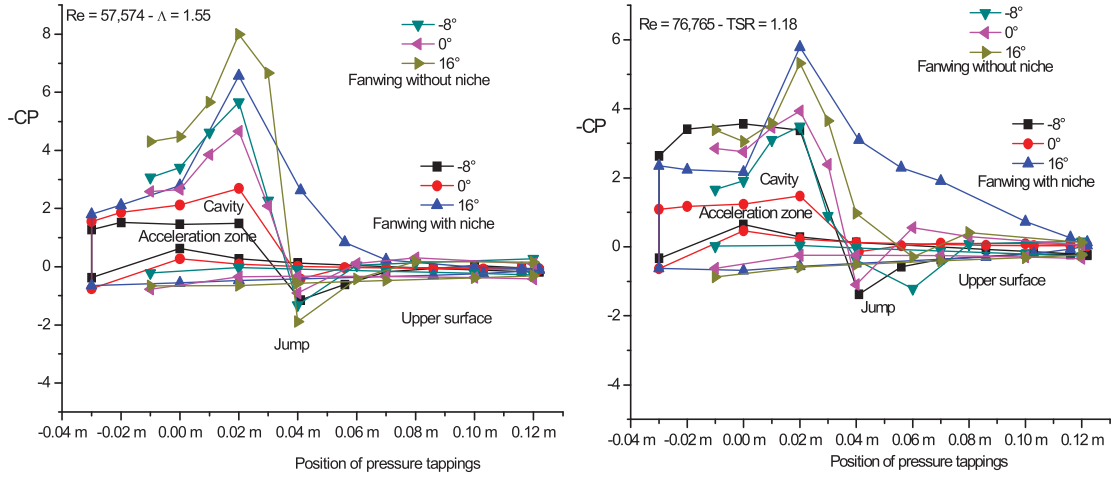

Figure 11. Comparison of the distribution of the pressure coefficient between the two profiles.

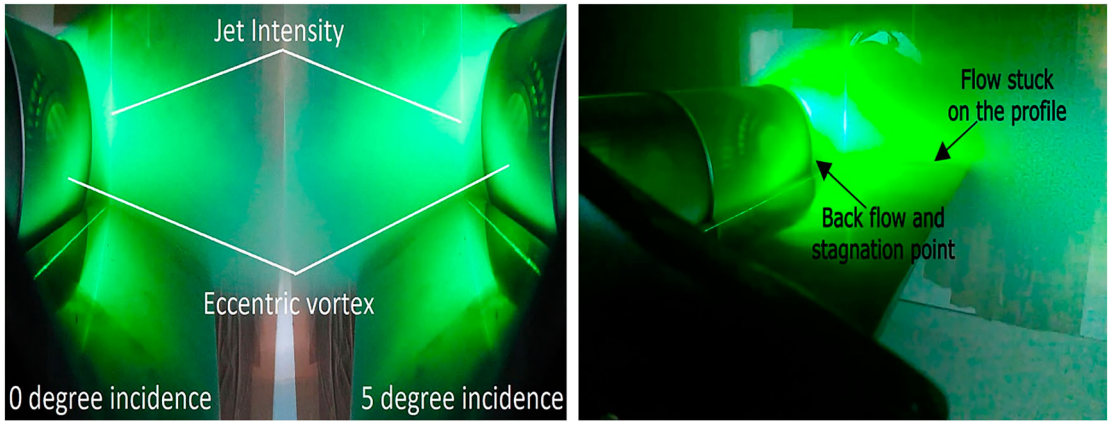

(a) (b)

Figure 12. Visualization of the flow in the closed test section. (a) Zero degrees (0°) and five degrees (5°). (b) Stagnation point and the flow attached on the upper surface.

which revitalizes the flow. The fluid contracts as it moves through the blades of Cross Flow Fan where most of the lift and propulsion occur then exits through the discharge fan, creating a wake behind the fan above the upper surface.

Figure 12(b) gives the topology of the wake behind the fan and on the upper surface. Also, the smoke highlights the development of the intensity of the flow. The color enhancement shows visualization where the smoke has been injected in order to see the flow regions by presenting the trajectory on the profile. It should be noted that the vanes are masked by the end support of the test bench. It can be seen that the position of the eccentric vortex straddles the vanes of the Cross-Flow Fan as well as the behavior of the wake flow after the discharge fan.

The direct impact of this result is observed on the curves of the pressure coefficient and the graphs of the lift coefficient. The flow is entirely attached on the upper surface of the profile. It indicates the intensity of the flow field and the recirculation at the stagnation point.

3. Numerical solution

The comparison of the numerical results with the experiment will concern the lift, drag and pressure coefficient. In order to analyze the behavior of the profiles, a two-dimensional (2D) unsteady numerical calculation of the Navier-Stokes equations was carried out on the domain. The ANSYS Fluent 6.3.26 solver is used to solve Navier-Stokes equations performed on Fanwing profiles associated with a rotating cross-flow fan. Figure 13(a) shows the domain and the mesh geometry of the Fanwing profiles. The field is divided into two parts; the first is the stator, which contains the wing, and the second is the rotor, containing the fan and the rotating field. They are connected by an interface, fluid-fluid so that the continuity of the flow is satisfied.

The size of the computational domain, upstream Profile [−11.5c *12.5c*−12.5c] and downstream profile [21c*12.5c*−12.5c], with a total meshes of 158,715 and 133,654 respectively of Fanwing with niche and without

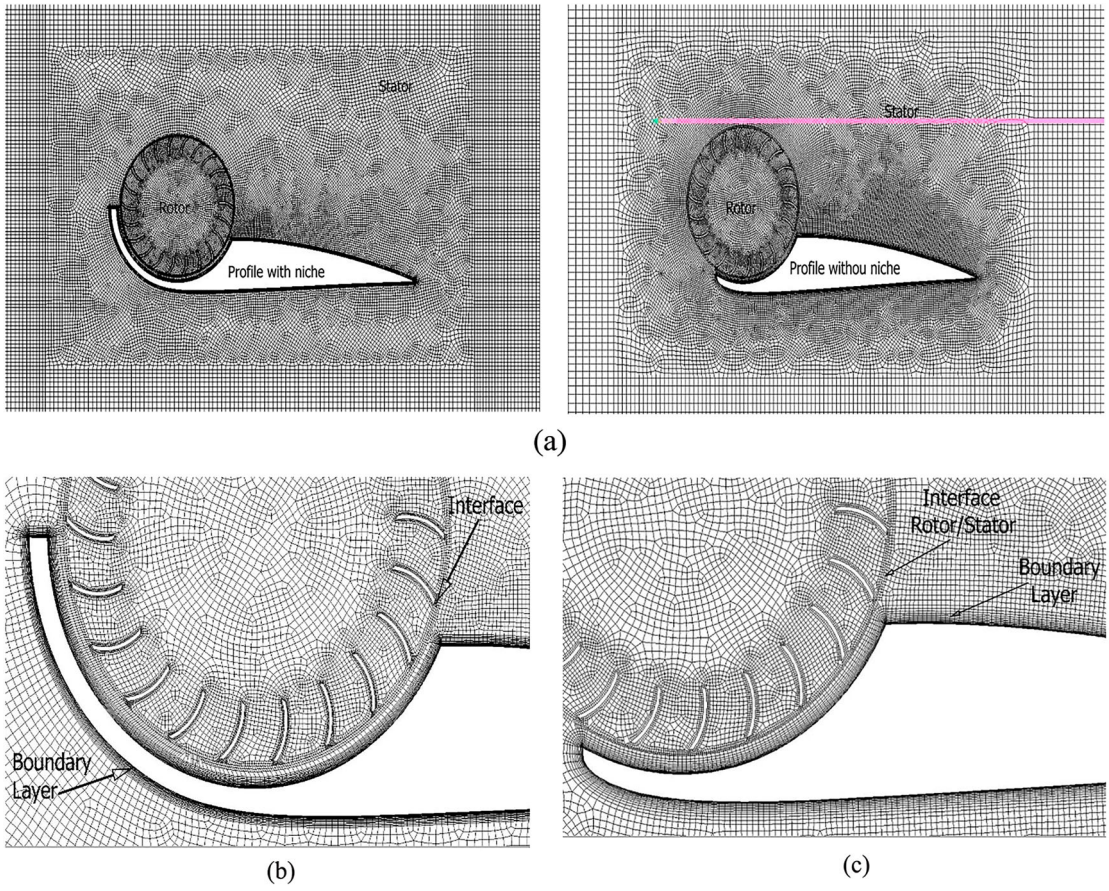

Figure 13. General view of the computational domain. (a) Computational domain. (b) The computational domain near the airfoil with niche. (c) The computational domain near the airfoil without niche.

niche, as well as the concentration of elements on the rotor blades of the central zone. To ensure an operating point of the simulation and to achieve a solution close to reality a condition is given to the input and output limits. A velocity condition at the inlet is imposed as well as pressure at the outlet. These conditions are not exactly compatible with the reality of flow; they are applied far from the study areas.

4. Schemes and boundary conditions

The SIMPLEC algorithm is applied for pressure-speed coupling. The discretization scheme of convective terms is of the second order. The finite volume method was applied to the mesh size of the calculation domain (Patankar, 1980; Versteeg & Malalasekera, 1995).

The two areas of computing (stator and rotor) are meshed with rectangular cells. In Figure 13(b,c) are showing the mesh of the flow field near the walls of the profile and the fan. Using the resolution of the sliding meshes, the simulation starts with a steady state for five hundred iterations, then switches to an unsteady calculation with a time step $\Delta t = 0.000909$ s, which is equivalent to a blade turn.

The position of $y+$ (nondimention wall distance) must check the condition $15 \leq y+ \leq 140$.

We have adapted the mesh for the fan to decrease the value of $y+$ since it has not been refined near the blades, which has resulted in a four percent (4%) improvement in lift.

5. Grid sensitivity analysis

The sensitivity test was performed on three mesh configurations. The convergence criteria of our study are the lift and drag coefficients. The Figure 14 below shows the evolution of C_L and C_D for the Reynolds number $Re = 57{,}574$ depending on the number of meshes at 0° incidence and a simulation time of 10 h for each profile. The intermediate mesh is chosen for reasons of saving calculation time by estimating the error of 1.5% for the C_L and about 3% for the C_D.

6. Transport equations and turbulence model

Continuity equation

$$\frac{\partial \rho}{\partial t} + \frac{\partial}{\partial x_i}(\rho u_i) = 0 \tag{5}$$

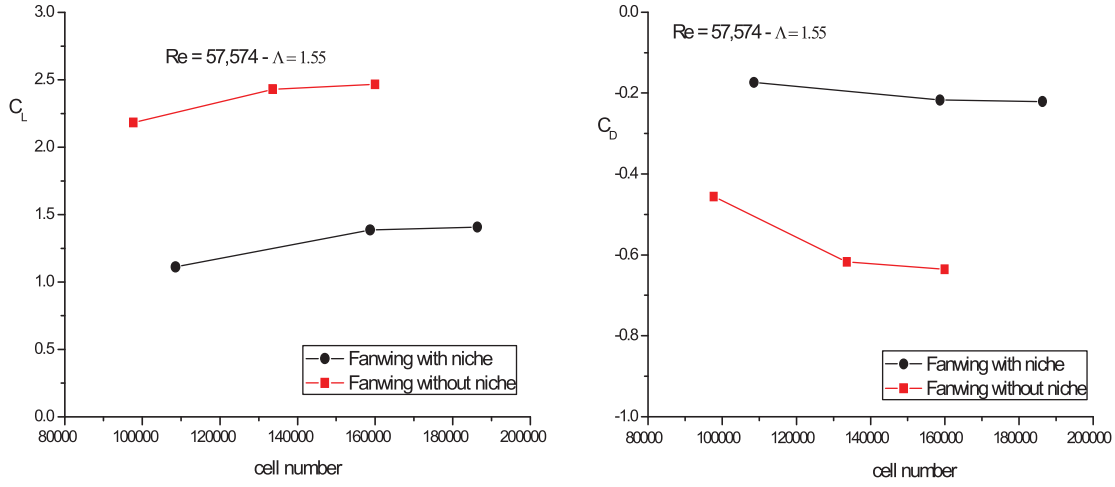

Figure 14. The sensitivity of the grid.

Momentum conservation equation

$$\frac{\partial}{\partial t}(\rho u_i) + \frac{\partial}{\partial x_j}(u_i u_j) = -\frac{\partial p}{\partial x_i} + \frac{\partial}{\partial x_j} \times \left[\mu\left(\frac{\partial u_i}{\partial x_j} + \frac{\partial u_j}{\partial x_i} - \frac{2}{3}\delta_{ij}\frac{\partial u_i}{\partial x_i}\right)\right] + \frac{\partial}{\partial x_i}(-\rho\overline{u'_i u'_j}) \tag{6}$$

where $(-\rho\overline{u'_i u'_j})$ Reynolds stress tensor that must be modeled for system closure.

The modeling is based on Boussinesq's hypothesis, which uses turbulent viscosity μ_t to link the Reynolds tensor components to the gradient of the mean velocity field. The idea of turbulent viscosity removes the problem of closure. Expressed by the following relationship.

$$-\rho\overline{u'_i u'_j} = \mu_t\left(\frac{\partial u_i}{\partial x_j} + \frac{\partial u_j}{\partial x_i}\right) - \frac{2}{3}\left(\rho k + \mu_t\frac{\partial u_i}{\partial x_i}\right)\delta_{ij} \tag{7}$$

where $\tau_{ij} = -\rho\overline{u'_i u'_j}$ Reynolds tensor; μ_t is the turbulent viscosity; k is the kinetic energy; $k = \frac{1}{2}(\overline{u'_i u'_j})$.

The advantage of this assumption is the considerable reduction in calculation costs.

The $k-\omega$ SST model is based on the transport of two equations, one for turbulence kinetic energy and one for vorticity:

$$\frac{\partial}{\partial t}(\rho k) + \frac{\partial}{\partial x_i}(\rho k u_i) = \frac{\partial}{\partial x_j}\left[\Gamma_k\frac{\partial k}{\partial x_j}\right] + G_k - Y_k + S_k \tag{8}$$

$$\frac{\partial}{\partial t}(\rho\omega) + \frac{\partial}{\partial x_i}(\rho\omega u_i) = \frac{\partial}{\partial x_j}\left[\Gamma_\omega\frac{\partial \omega}{\partial x_j}\right] + G_\omega - Y_\omega + D_\omega + S_\omega \tag{9}$$

One of the strengths of the SST model is the formulation of turbulent viscosity. The principle is based on the experimental observation of the turbulent shear ratio, $-(u'v')^{\sim}$, and turbulent kinetic energy. Thus, in much of the boundary layer, the ratio $\frac{-\widetilde{u'v'}}{k} \approx 0.31$. This condition, testing Bradshaw's hypothesis (FLUENT 6.3 Documentation) allows us to write:

$$\upsilon_t = \frac{0.31k}{\max(0.31\omega, |\Omega|F_2)} \tag{10}$$

with:

$$|\Omega| = \sqrt{2\Omega_{ij}\Omega_{ij}}$$

$$\Omega_{ij} = \frac{1}{2}\left(\frac{\partial U_i}{\partial x_j} - \frac{\partial u_j}{\partial x_i}\right)$$

Ω_{ij}: Is the average tensor of the rotation rate. Ω_1: Represents the Wilcox model constants and Ω_2 the k–ϵ model constants, then the mixed constants of the SST–k–ω model are defined by

$$\Omega = F_1\Omega_1 + (1 - F_1)\Omega_2 \tag{11}$$

6.1. Results and discussion

The unsteady flow is observed on the lift and drag coefficients. A total of ten hours was required to perform the 43,000 iterations needed to achieve convergence with an accuracy of 10^{-6} ddp. Convergence is the state where the residues remain unchanged.

The calculations were performed using an i5 CPU with 8 Giga RAM.

The CFD results predict that the lift coefficient (Figure 15) increases with the angle of attack up to $\alpha = 16°$, then the lift falls without stalling. The negative drag (Figure 16) defines the propulsion force. It weakens from $\alpha = 16°$, which requires us to develop more energy

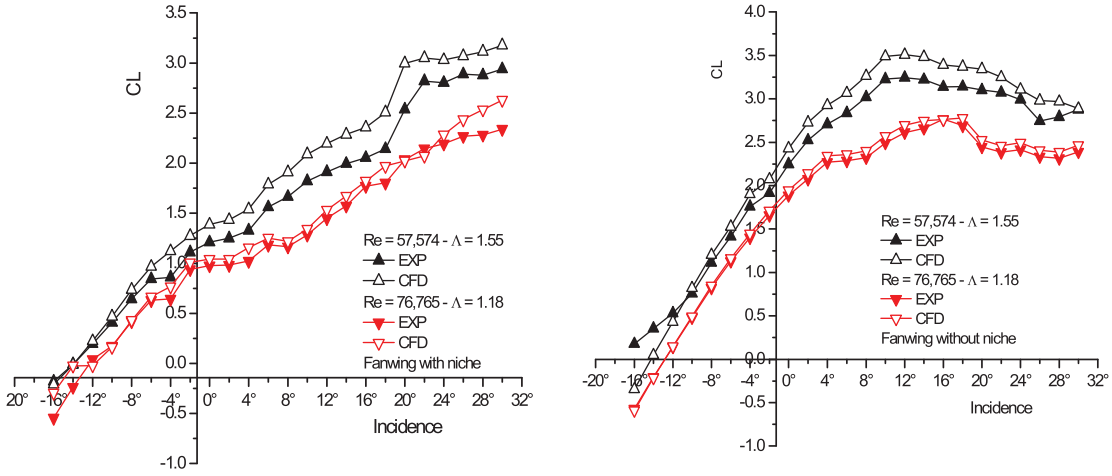

Figure 15. Comparison experimental and numerical lift coefficient of the profile.

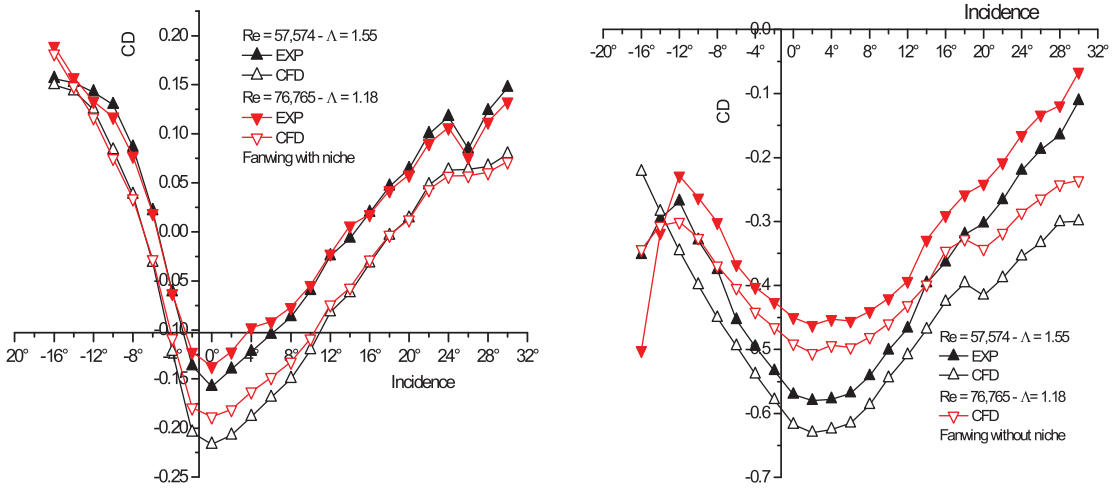

Figure 16. Comparison experimental and numerical drag coefficient of the profile.

to maintain vital propulsion. The lift and drag coefficients decrease with Reynolds number.

It is very difficult to accurately approximate and match exactly with high precision, experimental and numerical results. This can be attributed to:

(a) The uncertainty in the measurements, either in:
  (1) The angles of attack settings,
  (2) The fluctuation of the flow velocity,
  (3) The vibrations in fan due to the fan's rotating motor that creates wing oscillations.
(b) The convergence accuracy of the numerical solution and the airflow in three dimensions in the wind tunnel.

The aerodynamic parameters was predicted by the CFD and compared to the experimental data of the lift and drag coefficients shown in Figures 15 and 16 respectively, are close and in acceptable agreement. The aerodynamic coefficients were compared at one rotational speed and two Reynolds numbers, $Re = 57{,}574$ and $Re = 76{,}764$ that is $\Lambda = 1.18$ and $\Lambda = 1.55$. The error between the experimental values and the CFD values in Table 1 shows that the lift coefficient is about 9.25% and 16.65%. In addition, the drag is about 13.27% and 27.2%, for the profile without niche and profile with niche for a $\Lambda = 1.18$.

Table 1. Comparison of the coefficients of lift and drag experience and simulation at $\alpha = 4°$ incidence.

	Re = 57,574 – Λ = 1.55			Re = 76,765 – Λ = 1.18		
	EXP	CFD	Error %	EXP	CFD	Error %
Fanwing without niche						
CL	2.99093	3.29604	9.25	2.53998	2.84356	10.67
CD	−0.75209	−0.62685	16.65	−0.74894	−0.67876	9.37
Fanwing with niche						
CL	1.75542	2.02409	13.27	1.71329	1.8372	6.74
CD	−0.21668	−0.15773	27.2	0.116601	0.133158	12.43

It appears that the error decreases with the increase in the Reynolds number. For a $\Lambda = 1.55$, it indicates 10%

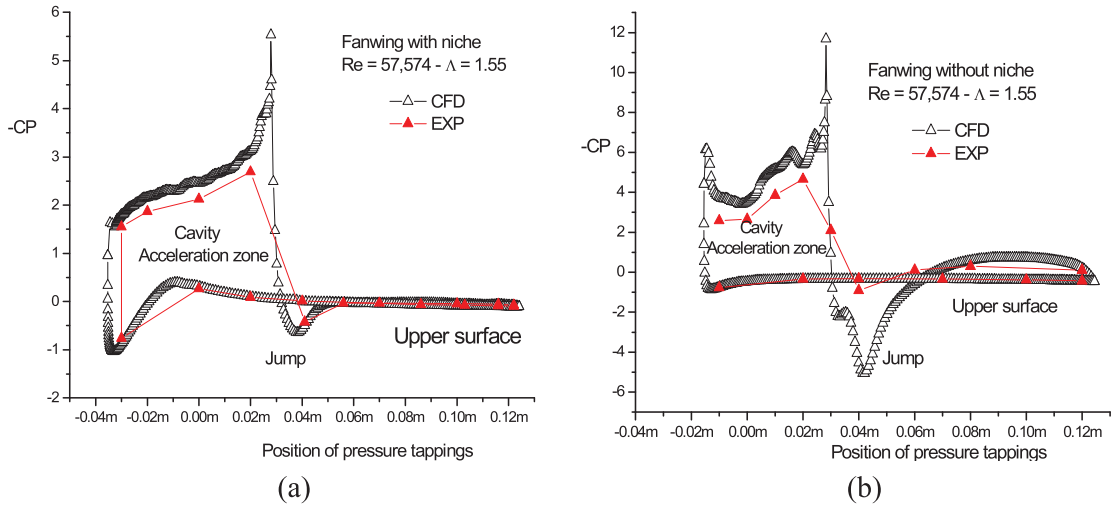

Figure 17. Distribution of the pressure coefficient at $\alpha = 0°$.

and 6.74%, for the lift and 12.4% and 9.37%, for the drag of the profiles with and without niche. The error of the lift coefficient is small compared to the drag coefficient, because the drag force is generally difficult to predict precisely.

Figure 17 shows the distribution of the pressure coefficient at $\alpha = 0°$. Overall, even though they are similar in shape, we see that the Fanwing with niche does not develop an interesting pressure gradient, unlike the Fanwing without niche, which is considerable all along the profile. It is reflected in the lift. The sudden surge of pressure on the upper surface of the profile is due to the geometry of the cavity of the profile and the sharp edge. To reduce this jump, Askari and Shojaeefard (2015) stated to replace the sharp edge by a smooth and round edge.

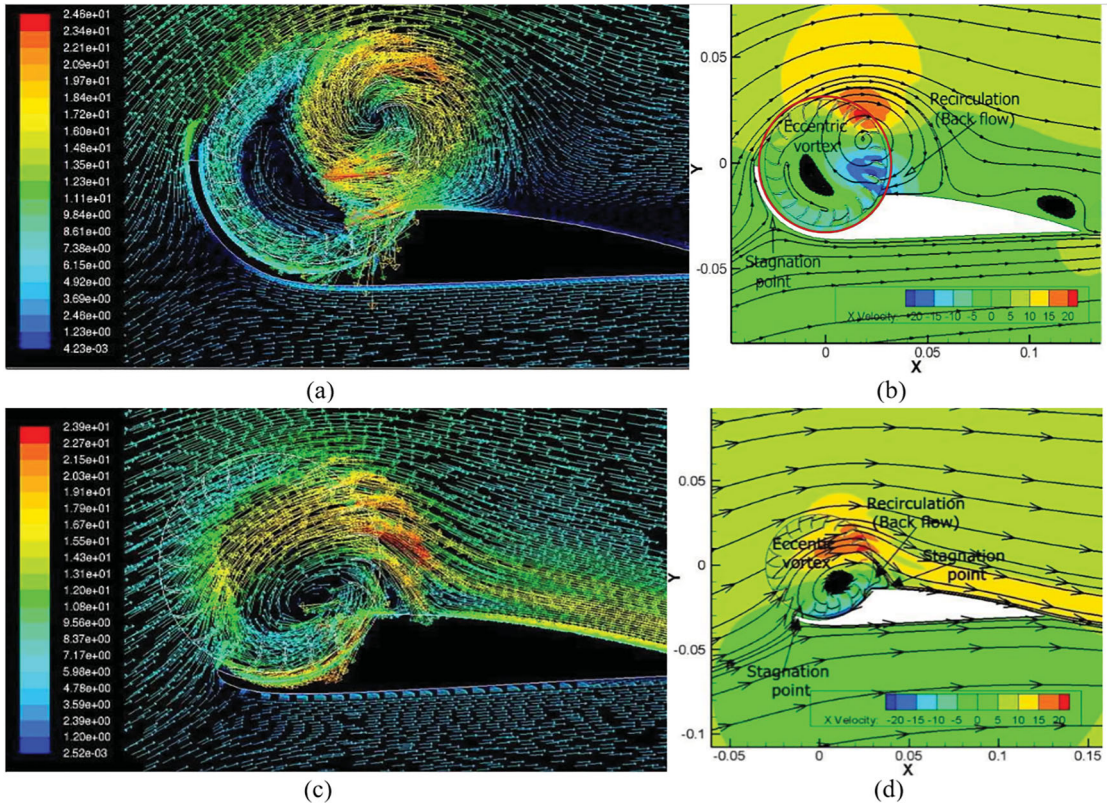

Figure 18. Comparison of flow between profiles. (a) Velocity vector near wall of Fanwing profile with niche. (b) Streamlines around the Fanwing profile with niche. (c) Velocity vector near wall of Fanwing profile without niche. (d) Streamlines around the Fanwing profile without niche.

6.2. Flow analysis

Figure 18(b,d) show that the streamlines are very close to each other on the upper surface, compared to the lower surface. This indicates a low speed and high pressure on the latter. The speed gradient on the upper surface increases with the Reynolds number, which gives more friction.

The influence of geometry on the flow topology between the fanwing with and without niche is noticeable. The eccentric vortex is highlighted and is influenced by the recirculation of the partial flow associated with the impact of the forced flow of the vector velocity striking the profile, which constitutes a considerable loss of energy.

The swirling air penetrates frontally, before being redirected in the tangential direction of the fan. A pressure difference is created between the internal zone and the discharge zone, which causes part of this airflow to return through the clearance between the fan and the niche, which creates recirculation. (Figure 18(a,c)).

For the 4° incidence, the recirculation becomes sharp, giving rise to two lobes on the top surface of the profile with recess and on the fan. The air is sucked in on the discharge side and swirls creating a depression between the top surface and the fan (the flow presents a disorganization of the current lines where the flow remains trapped and rotating inside the rotor). The geometric shape of the niche increases the drag and reduces propulsion.

The morphology of the flow through the rotor and stator shows the manifestation of two stagnation points on the profile, the first one facing the leading edge and the second one on the upper surface at the fan outlet. The recirculation is strongly visible by the back flow to the interior of the cavity. This phenomenon is more apparent on the profile with a niche.

The most remarkable fact is the flow on the Fanwing with niche. There is the appearance of a large lobe high in intensity that affects the system that no longer develops propulsion unlike the profile without niche. We observe almost all the flow ejected and transformed into propulsion with a tiny return of the back flow. It appears that on the profile without a niche, the fan prevents the flow separation.

7. Conclusion and future work

Aeronautics has been using cross-flow fans as propulsion equipment for some years. Even if they develop with difficulty, their potential has enabled the Fanwing their implementation.

For two Reynolds numbers and two Tip Speed Ratio, the two Fanwing models with different profiles of infinite scale, have been studied numerically and experimentally. The aerodynamic performance of the system resulted in a high lift coefficient. However, the geometry of the niche influences the flow. It was observed that the drag could be felt because of it.

The experimental study made it possible to quantify the global and local performances of the profiles. The analysis shows that as the Reynolds number increases, as well as the aerodynamic forces of the profiles increase. On the other hand, the corresponding aerodynamic coefficients decrease.

The fanwing without niche yielded results that are more interesting with more lift and propulsion. Unlike the fanwing with niche where they were weak. For the numerical approach, the aerodynamic parameters and the flow field are analyzed. The URANS simulation made it possible to observe the topology of the internal flow.

The modeling reveals the internal flow's appearance contributes to its visualization, and confirms its complexity. The interaction between the rotor and stator shows an eccentric vortex inside the rotor generated by the rotation of the Cross-Flow Fan and a recirculation giving rise to a point of stagnation caused by a back flow, which gives a loss of energy. In addition, the Fanwing without a niche does not seem to stall, even if the lift decreases. This is due to the accelerated airflow which prevents separation.

Nevertheless, there is a need to vary the speed of rotation, which should also be studied on the effects of air compressibility at the blades.

The most interesting improvement is the addition of a mobile perforated deflector covering the Cross-Flow Fan profile without niche. It protects the Cross-Flow Fan from birds and helps to control the airflow and reduce the back flow.

The continuation of our research and future work will focus on 'The boundary layer effect on the aerodynamic parameters of fanwing profile', which is currently under study and will be submitted to the journal shortly. And the influence of the cross flow fan diameter on the air flow behavior 'Optimization of the cross flow-fan diameter with an acoustic study'. Future work should also focus on the addition of a mobile perforated deflector covering the cross-flow fan profile without niche, it protects the cross-flow fan from birds and helps to control the airflow and reduce the back flow because it's the most interesting improvement.

Disclosure statement

No potential conflict of interest was reported by the authors.

Funding

This work was supported by the Ministry of Education, Youth and Sports Czech Republic, by the Specific research at Brno University of Technology [grant number FAST-J-19-5976].

ORCID

Ondřej Šikula http://orcid.org/0000-0002-7661-0732

References

Abbott, A. C., & Von Doehoff, A. E. (1959). *Theory of wing sections*. New York, NY: Dover publication.

Ahad, O., & Graham, J. M. R. (2007). Flight simulation and testing of the FanWing experimental aircraft. *Aircraft Engineering and Aerospace Technology*, *79*(2), 131–136.

Akbarian, E., Najafi, B., Jafari, M., Ardabili, S. F., Shamshirband, S., & Chau, K.-w. (2018). Experimental and computational fluid dynamics-based numerical simulation of using natural gas in a dual-fueled diesel engine. *Engineering Applications of Computational Fluid Mechanics*, *12*(1), 517–534. doi:10.1080/19942060.2018.1472670

Ardabili, S. F., Najafi, B., Shamshirband, S., Bidgoli, B. M., Deo, R. C., & Chau, K.-w. (2018). Computational intelligence approach for modeling hydrogen production: A review. *Engineering Applications of Computational Fluid Mechanics*, *12*(1), 438–458. doi:10.1080/19942060.2018.1452296

Askari, S., & Shojaeefard, M. H. (2015). Experimental and numerical study of an airfoil in combination with a cross flow fan. *Proceedings of the Institution of Mechanical Engineers, Part G: Journal of Aerospace Engineering*, *227*(7), 1173–1187.

Chen, Y., & Lian, Y. (2015). Numerical investigation of vortex dynamics in an H-rotor vertical axis wind turbine. *Engineering Applications of Computational Fluid Mechanics*, 21–32. doi:10.1080/19942060.2015.1004790

Douglas, A. R., & Geoff, E. L. (2009). *Effects of Fanwinging design on airfoil performance*. Los Angeles, CA: University of Southern California.

Duddempudi, D., Yao, Y., Edmondson, D., Yao, J., & Curley, A. (2007). Computational study of flow over generic fan-wing airfoil. *Aircraft Engineering and Aerospace Technology*, *79*(3), 238–244.

FLUENT 6.3 Documentation. Help User's Guide, Modeling Turbulence.

Forshaw, S. (1999). *Wind-Tunnel investigation of Fanwing*. London: Final Year Project, M.Eng. Imperial College.

Ghalandari, M., Koohshahi, E. M., Mohamadian, F., Shamshirband, S., & Chau, K.-W. (2019). Numerical simulation of nanofluid flow inside a root canal. *Engineering Applications of Computational Fluid Mechanics*, *13*(1), 254–264. doi:10.1080/19942060.2019.1578696

Harloff, G. J. (1979). *Cross-flow fan E experimental development and finite element modeling* (PhD., Dissertation). The University of Texas at Arlington.

Kentfield, J. A. C. (2005). *Drag reduction and improved fuel consumption of aircraft employing outboard horizontal stabilizers*. 43rd AIAA Aerospace Sciences Meeting and Exhibit, Aerospace Sciences Meetings.

Kogler, K. U. (2000). *FANWING, experimental evaluation of a novel lift & propulsion device* (M.Eng., Thesis). Imperial College, London.

Kummer, J. D. (2010). Propulsive wing "propulsive wing aerial utility vehicle development". *Dynamics Magazine*. Retrieved from http://www.cdadapco.com/press_room/dynamics/v301

Kummer, J. D., & Dang, T. Q. (2006). High-lift propulsive airfoil with Integrated cross-flow fan. *Journal of Aircraft*, *43*, 4.

Leroy, H., & Smith, J. (1993). Wake ingestion propulsion benefit. *Journal of Propulsion and Power*, *9*, 1.

Mazur, J. S. (1984). *A study of the cross-flow fan* (PhD., Dissertation). Wayne State University, Detroit, MI.

Moon, Y. J., Cho, Y., & Nam, H. (2003). Computation of unsteady viscous flow and aero acoustic noise of cross-flow fans. *Computers & Fluids*, *32*(7), 995–1015.

Mortier, P. (1893). United States Patent Office No.: US 1893/507445.

Mou, B., He, B.-J., Zhao, D.-X., & Chau, K.-w. (2017). Numerical simulation of the effects of building dimensional variation on wind pressure distribution. *Engineering Applications of Computational Fluid Mechanics*, *11*(1), 293–309. doi:10.1080/19942060.2017.1281845

Patankar, S. V. (1980). Numerical heat transfer and fluid flow. *Series in computational and physical processes mechanics and thermal sciences* (xiii, p. 197). Bristol, PA: Taylor & Francis.

Peebles, P. (2001). United States Patent. Patent Nº US 6,231.

Ramezanizadeh, M., Nazari, M. A., Ahmadi, M. H., & Chau, K.-w. (2018). Experimental and numerical analysis of ananofluidic thermosyphon heat exchanger. *Engineering Applications of Computational Fluid Mechanics*, *13*(1), 40–47. doi:10.1080/19942060.2018.1518272

Saracoglu, B. H., & Paniagua, G. (2015). *Analysis of the flow field around the wing section of a Fanwing aircraft under various flow conditions*. 53rd AIAA Aerospace Sciences Meeting.

Seyfang, G. R. (2011). *Recent developments of the Fanwing aircraft*. 3rd CEAS Air & Space Conference, 21st AIDAA Congress.

Tanaka, S., & Murata, S. (1994). Scale effects in cross-flow fans (effects of fan dimensions on performance curves). *JSME International Journal Series B – Fluids and Thermal Engineering*, *37*(4), 844–852.

Technical document of the wind tunnel type TE 44. *Department mechanical engineering, faculty mechanical engineering*. Oran: USTO.

Toffolo, A. (2005). On the theoretical link between design parameters and performance in cross-flow fans: A numerical and experimental study. *Computers & Fluids*, *34*(1), 49–66.

Versteeg, H. K., & Malalasekera, W. (1995). *An introduction to computational fluid dynamics: The finite volume method*. Harlow, Essex: Longman.